Advances in Aircraft and Spacecraft Science, *Vol. 12, No. 4 (2025) 387-418*
https://doi.org/10.12989/aas.2025.12.4.387

Failure assessment of SS304L-GI-EN24T dissimilar welded joints for application in milk transported tanker structure

Shivaji G. Chavan[1a], Milind B. Patil[1a] and D.N. Raut*[1,2]

[1]*Production Engineering Department, VJTI, Matunga, Mumbai, 400019, India*
[2]*VJTI Mumbai, Mumbai, Maharashtra 400019, India*

(Received February 6, 2025, Revised July 27, 2025, Accepted September 26, 2025)

Abstract. This study investigated the strengthening mechanisms and failure analysis of dissimilar welded joints between SS304L stainless steel and EN24T mild steel. The mechanical characteristics and tensile failure performance of the joints were evaluated. The microstructures of different joint configurations (MS-MS, MS-SS, SS-GI, and MS-GI) were first examined using SEM and EBSD analysis. Subsequently, tensile tests were conducted on four samples of these joints, which were prepared according to the ASME E8 standard. The MS-SS dissimilar welded joint exhibited the maximum load capacity of 35.71 KN, while the SS-GI joint showed the minimum capacity of 27.49 KN. The effects of weld thickness and specimen length on the strength of the joint structure were also studied. A Finite Element Method (FEM) model was developed for all cases and validated against the experimental results. The proposed FEM model shows very good agreement with the experimental data. The yield strengths of the dissimilar metal joints, as obtained from the UTM, were 320 MPa for MS-MS, 384 MPa for MS-SS, 343 MPa for MS-GI, and 325 MPa for SS-GI. This research demonstrates that the dissimilar metal weld joint, particularly the MS-SS configuration, is an effective and suitable choice for application in milk tanker structures.

Keywords: dissimilar weld failure analysis; FEM; fractography; tensile test

1. Introduction

Due to their excellent corrosion resistance and mechanical properties, welded joints between SS304L and EN24T are widely used in various industries, including dairy, petrochemical, and aerospace. For instance, in milk tankers, a stainless steel (SS) tank is often joined to a mild steel (MS) chassis using a dissimilar welded joint. Researchers have extensively studied the integrity of such structures. Okada *et al.* (2016) developed an automated analysis procedure to perform parametric studies on crack shapes and loading conditions in welded joints. Furthermore, Kyaw *et al.* (2023) studied the fractured surfaces of welded zones resulting from thermal loading. These thermomechanical phenomena during fabrication can lead to significant variations in product properties, particularly in metallographic characteristics, as investigated by Pal *et al.* (2024). Tian *et al.* (2023) presented the role of retained austenite and multi-orientation microstructures as a supplement to existing pearlite wheels. Their study also identified heat-affected zones on pearlite

*Corresponding author, Professor, E-mail: shivajigchavan@gmail.com
[a]Ph.D.

http://www.techno-press.org/aas/8 ISSN: 2287-528X (Print), 2287-5271 (Online)

and bainitic wheel treads, noting that several severe failure cracks were found in both, particularly in the pearlite ones. Langari *et al.* (2023) investigated the impact of welding input parameters—such as tool rotational speed, welding speed, shoulder radius, and tool geometry—on weld joint quality, including strength, toughness, hardness, fractography, and fatigue behavior. Concurrently, Zheng *et al.* (2024) studied the failure mechanism of steel frames with angle steel-bolted connections exposed to fire under progressive collapse conditions. Baskaya *et al.* (2024) investigated surface characteristics and high-temperature fatigue performance. In their research, they also studied the effects of different Severe Plastic Deformation (SPD) process durations on the surface morphology, microhardness, and residual stress of the weld joints. In a separate study, Feizollahi and Moghadam (2024) examined the degradation on the surfaces of electrodes used in the resistance spot welding of hot-dip galvanized and galvanize low-carbon steels and tested electrode life.

Research into the behavior and welding of steel and aluminum alloys continues to advance through a combination of experimental and simulation techniques. Recent studies have employed various methods to characterize material properties and welding outcomes. For instance, Liu *et al.* (2024) investigated the passive and pitting behaviors of multiphase stainless-steel using Auger electron spectroscopy, X-ray photoelectron spectroscopy, atomic force microscopy, and electrochemical techniques. Similarly, Raoelison *et al.* (2023) analyzed the transformation sequence of Mg-Si precipitates in an Al-Mg-Si alloy during magnetic pulse welding. On the structural mechanics front, Khater *et al.* (2024) studied the elastic distortional buckling of cold-formed steel Z-beams with stiffened holes, while Park *et al.* (2024), Zhang *et al.* (2024) examined the elastic nature and stress distribution of steel structures. Koubova (2024) developed a solution for yielding steel arch supports used in mining. In welding research, Chuaiphan *et al.* (2024) investigated the role of hydrogen in shielding gas for the gas tungsten arc welding (GTAW) of dissimilar stainless-steel joints, and Prabhu *et al.* (2022) explored how post-weld heat treatments improve the mechanical behavior of friction stir welded (FSW) dissimilar aluminum alloys. Given the complexities of welding, modeling is highly desirable to predict component deformation, residual stresses, and metallurgical changes before physical manufacture. This was highlighted by Tirenifi *et al.* (2019). Examples of such modeling include the work of Matuszewski (2018), who modeled the 3D temperature field in a butt-welded joint using ANSYS, and Mikolasek *et al.* (2018), who conducted a numerical and experimental analysis of welds in steel structural elements. However, advanced welding processes like laser beam welding present challenges, including the optimization of process parameters, experimental setup, handling requirements, and high costs. To minimize the need for complex and expensive physical experiments, Finite Element Method (FEM) simulation techniques are increasingly employed to estimate heat input and optimize the welding process prior to experimental validation.

Various authors have focused on stainless steel welded joints. However, the specific problem of an SS304L-GI-EN24T welded joint has not yet been investigated. This article presents a failure assessment of SS304L-GI-EN24T dissimilar welded joints for application in milk tankers, as shown in Fig. 1. The study investigated the mechanical characteristics and tensile failure performance of the welded joints. Initially, the effects on the microstructure (analyzed via SEM and EBSD) and the resulting mechanical properties of different joint configurations—MS-MS, MS-SS, SS-GI, and MS-GI—were studied. Subsequently, tensile tests were conducted on four samples of these welded joints (MS-MS, MS-SS, SS-GI, MS-GI), which were prepared according to the ASME E8 standard. The evidence demonstrates the substantial potential of the proposed SS-MS-GI dissimilar welding method for the accurate failure assessment of such welds in commercial applications, specifically for milk transport tanker structures.

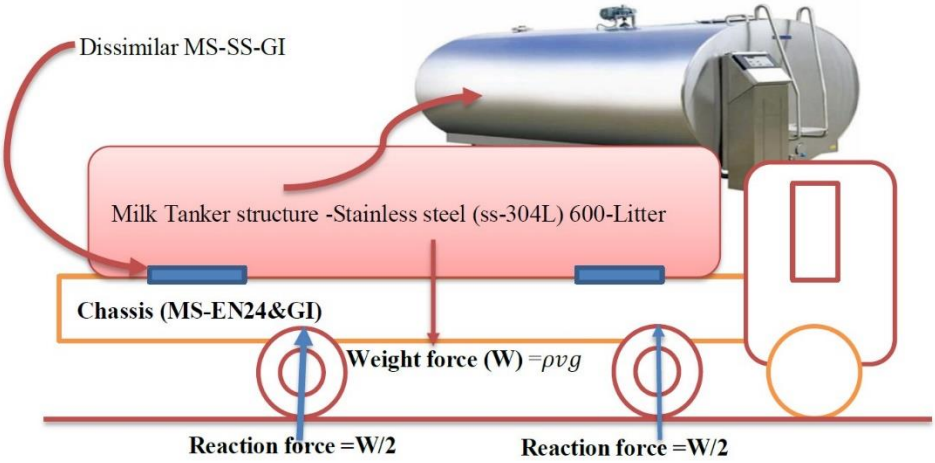

Fig. 1 Actual application of SS-MS-GI dissimilar welded joint in milk-transported structure

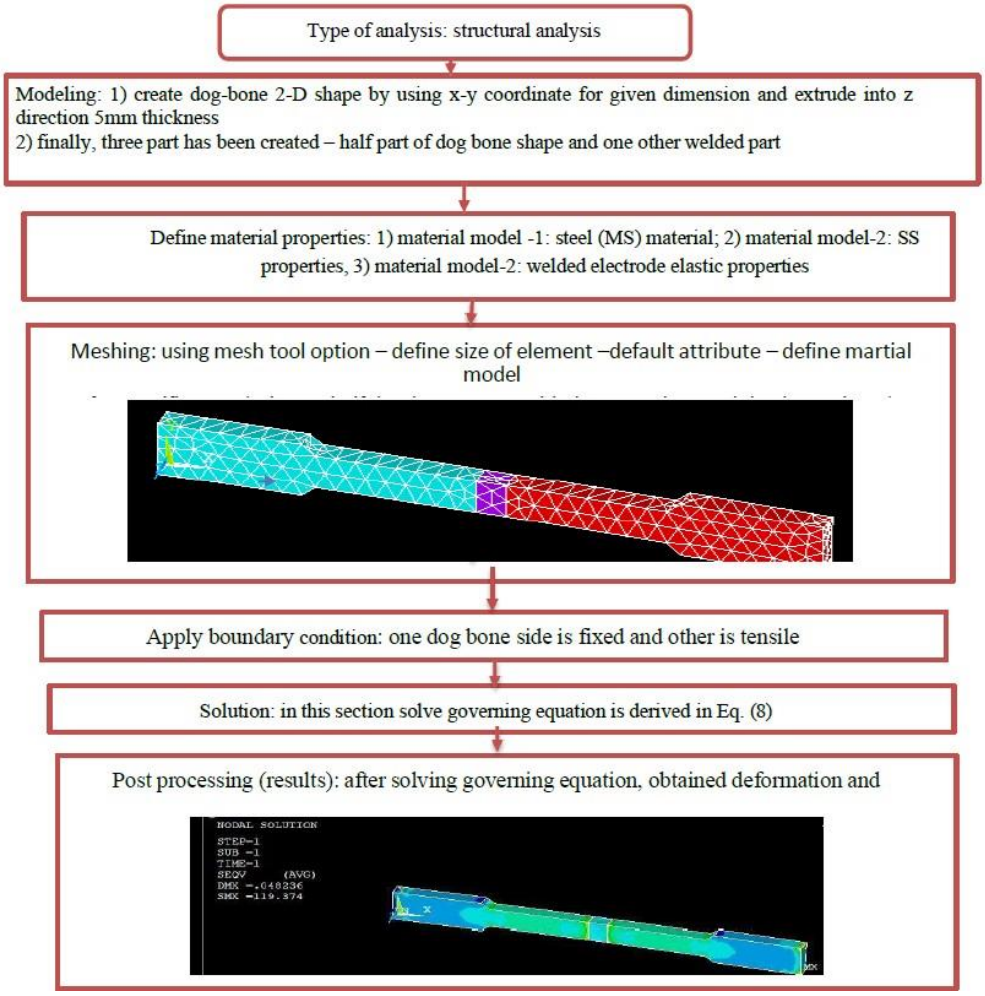

Fig. 2 Flow chart for ANSYS stapes for simulation of dissimilar welded joint structure

2. 3-D finite element simulation procedure for dissimilar welded joint:

The stepwise procedure for dissimilar welding joint FEM process is given in flow chart as following Fig. 2 flow chart for FEM analysis of dissimilar welded joint.

Computation of shape function

The deformation of the dissimilar butt weld joint is defined by its displacements in the *x*, *y*, and *z* directions. A corresponding shape function for the 3D Finite Element Model (FEM) was developed as follows (Okada *et al*. 2016).

The displacement field for dissimilar welded joints is defined as

$$u(x,y,z)=\text{Ni UI} \tag{1}$$

Displacement field for dissimilar metal welded joint is defined as: Strain energy can be written as

$$\Delta=\frac{1}{2}\int_v [\sigma]\varepsilon^T dv \tag{2}$$

The external work of dissimilar welded joint is defined

$$\text{w}=\left\{\iiint_{(x,y,z)}^{L,w,h}[N]^T\{P(x,y,z)\}dv\right\}\{u(x,y,z)\} \tag{3}$$

Total protentional energy of different type of welded joint due to tensile loading is given by Eq. (4)

$$\pi=\Delta-w \tag{4}$$

Potential energy can be written as

$$\pi=\frac{1}{2}\int_v [\sigma]\varepsilon^T dv-\left\{\iiint_{(x,y,z)}^{L,w,h}[N]^T\{P(x,y,z)\}dv\right\}\{u(x,y,z)\} \tag{5}$$

Minimum protentional energy approach has been employed for dissimilar butt welded joint, by

$$\frac{\partial\pi}{\partial u(x,y,z)}=0 \tag{6}$$

3-D welded model of protentional energy with respective deformation is zero and solve Eq. (6)

$$\frac{\partial\left\{\frac{1}{2}\int_v [\sigma]\varepsilon^T dv-\left\{\iiint_{(x,y,z)}^{L,w,h}[N]^T\{P(x,y,z)\}dv\right\}\{u(x,y,z)\}\right\}}{\partial u(x,y,z)}=0 \tag{7}$$

After Solving we get, governing equation for find unknown deformation of dissimilar welded joint.

$$[K]\{u\}=\{P\} \tag{8}$$

Where, [*K*]=stuffiness matrix system of equation, *P*=tensile load vector for welded joint

$$[k]=\sum_{n=1}^{m}\left[\int_v([B(x,y,z)]^T[C][B(x,y,z)])dv\right]_e^m$$

$$P=\left\{\iiint_{(x,y,z)}^{L,w,h}[N]^T\{P(x,y,z)\}dv\right\}$$

The deformation of all nodal solution of each element is given by

$$u(x,y,Z) = \{P\}[K]^{-1} \tag{9}$$

Strain of all element is defined as

$$\varepsilon(x,y,z) = \frac{u(x,y,z)}{(X,Y,Z)} \tag{10}$$

Strass can be obtained Eq. (23) for SS, MS and GI material by using Eqs. (10)-(13)

$$\sigma(x,y,z)_{SS,MS,GI} = E_{SS,MS,GI}\varepsilon(x,y,z) \tag{11}$$

Stress singularity can be written as

$$\text{Stress singularity}(\alpha) = \frac{\sigma_{von}}{\sigma_1} \tag{12}$$

3. Failure analysis for dissimilar welded joint due to tension

Present study is focused on dissimilar metal welded joint failure as ductile behavior; Hence the energy distortion failure theory was employed for dissimilar welded joint. The strain energy causing dissimilar weld failure, and distortion energy associated with the shared first invariant of deviatoric stress equal to zero.

The state of stress is given by

$$[\sigma] = \begin{bmatrix} \sigma_1 & 0 & 0 \\ 0 & \sigma_2 & 0 \\ 0 & 0 & \sigma_3 \end{bmatrix} = \begin{bmatrix} \sigma_1 - p & 0 & 0 \\ 0 & \sigma_2 - p & 0 \\ 0 & 0 & \sigma_3 - p \end{bmatrix} + \begin{bmatrix} p & 0 & 0 \\ 0 & p & 0 \\ 0 & 0 & p \end{bmatrix} \tag{13}$$

First, invariant

$$\text{I0} = \sigma_1 - p + \sigma_2 - p + \sigma_2 - p \,\&\, p = \frac{1}{3}\sigma_{ij} \tag{14}$$

Volumetric strain is defined as

$$\varepsilon_v = \varepsilon_1 + \varepsilon_2 + \varepsilon_3 \tag{15}$$

$$\varepsilon_v = \frac{1}{E}\{(\sigma_1 + \sigma_2 + \sigma_3) - 2\vartheta(\sigma_1 + \sigma_2 + \sigma_3)\} \tag{16}$$

$$\varepsilon_v = \frac{(1-2\vartheta)}{E}(\sigma_1 + \sigma_2 + \sigma_3) = \frac{(1-2\vartheta)}{E}p \tag{17}$$

Volumetric strain energy for dissimilar welded joints is defined as: *Uv*=(hydrostatic pressure) (volumetric strain)

$$CapU_v = \frac{1}{2}\varepsilon_v p = \frac{(1-2\vartheta)}{6E}p^2 = \frac{(1-2\vartheta)}{6E}(\sigma_1 + \sigma_2 + \sigma_3)^2 \tag{18}$$

Strain energy for principle -stress-strain is given by

$$U = \frac{1}{2E}(\sigma_1^2 + \sigma_2^2 + \sigma_3^2) - \frac{\vartheta}{E}(\sigma_1\sigma_2 + \sigma_2\sigma_3 + \sigma_3\sigma_1)$$

Distortion energy is defined for welded joint

$$Ud = U - U_v \tag{21}$$

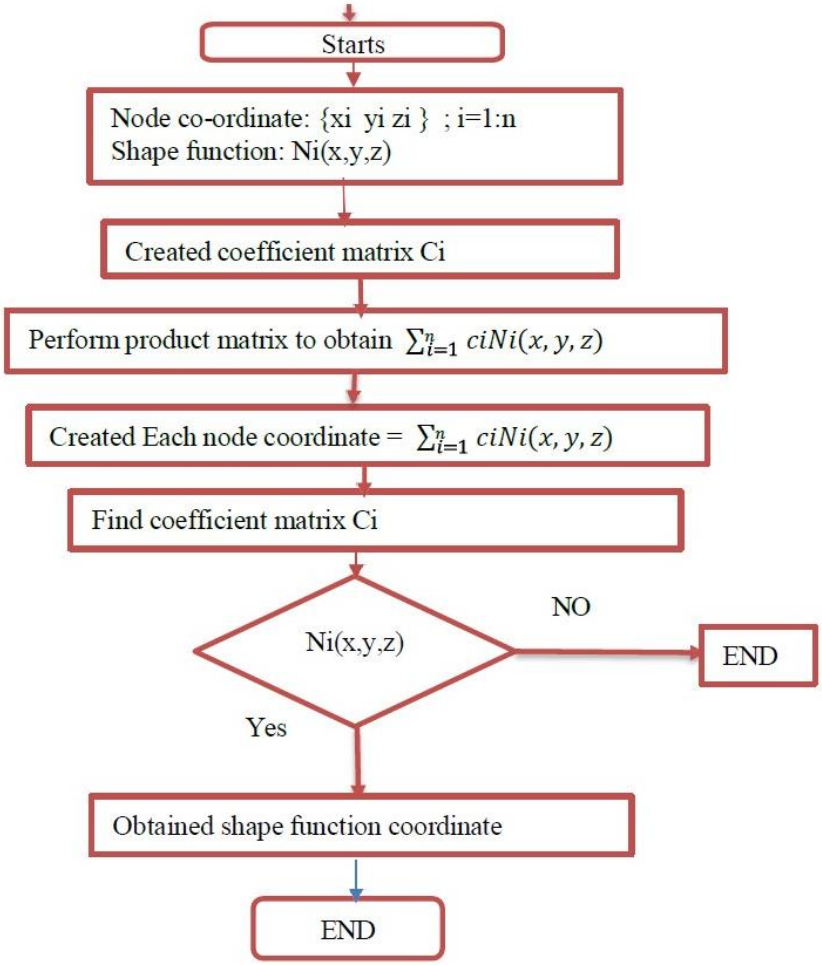

Fig. 3 shape function generation algorithms

$$Ud = \frac{1}{2E}(\sigma_1^2 + \sigma_2^2 + \sigma_3^2) - \frac{\vartheta}{E}(\sigma_1\sigma_2 + \sigma_2\sigma_3 + \sigma_3\sigma_1) \quad -\frac{(1-2\vartheta)}{6E}(\sigma_1 + \sigma_2 + \sigma_3)^2 \tag{22}$$

$$capsUd = \frac{1}{12G}[(\sigma_1 - \sigma_2)^2 + (\sigma_2 - \sigma_3)^2 + (\sigma_3 - \sigma_1)^2] \tag{23}$$

$$Ud = \frac{Y^2}{6G} = \frac{1}{12G}[(\sigma_1 - \sigma_2)^2 + (\sigma_2 - \sigma_3)^2 + (\sigma_3 - \sigma_1)^2] \tag{24}$$

$$2Y^2 = (\sigma_1 - \sigma_2)^2 + (\sigma_2 - \sigma_3)^2 + (\sigma_3 - \sigma_1)^2 \tag{25}$$

$$Y^2 = \frac{1}{2}(\sigma_1 - \sigma_2)^2 + (\sigma_2 - \sigma_3)^2 + (\sigma_3 - \sigma_1)^2 \tag{26}$$

$$\left(\frac{\sigma_1}{Y}\right)^2 + \left(\frac{\sigma_2}{Y}\right)^2 - \left(\frac{\sigma_{1\sigma_1}}{Y^2}\right) = 1 \tag{27}$$

Complete stress envelops of von-Mises and Tresca criteria for dissimilar welded joint as shown Fig. 4.

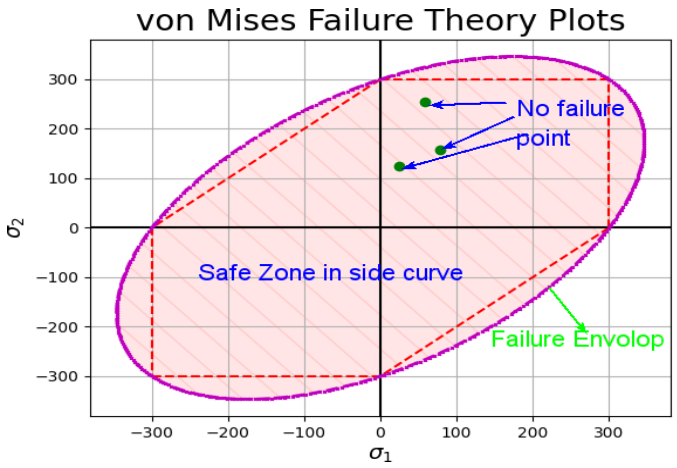

Fig. 4 The failure s envelope Von Mises and Tresca Failure Criterion for dissimilar butt-welded joints subjected to tension

	A	B	C	D	E	F	G	H	I
5									
6	Axial Displ	Axial Force	Time	Extensometer	Area	Stress	Modulus	offset strain	Offset strass
7	mm	kN	sec	mm/mm			slop		
8	0.0012786	0.218686646	0.17985	-1.25E-06	67.36	3.246536	218497.4	2.00E-03	4.37E+02
9	0.0059481	0.310745026	0.229818	4.25E-05		4.613198		2.04E-03	4.45E-01
10	0.0036535	0.491183441	0.279785	-6.59E-06		7.291916		1.99E-03	4.35E-01
11	0.0071893	0.632177002	0.329753	2.37E-05		9.385051		2.02E-03	4.41E-01
12	0.0081564	0.746815247	0.37972	-2.07E-05		11.08692		1.98E-03	4.31E-01
13	0.0060375	0.844349976	0.429688	1.77E-05		12.53489		2.02E-03	4.40E-01
14	0.0105379	0.936062988	0.479655	-2.43E-05		13.89642		1.98E-03	4.31E-01
15	0.0097147	1.068498779	0.529622	1.91E-05		15.86251		2.02E-03	4.40E-01
16	0.0105647	1.16253186	0.57959	-3.44E-05		17.25849		1.97E-03	4.28E-01
17	0.0136852	1.245536255	0.629557	1.67E-05		18.49074		2.02E-03	4.40E-01
18	0.0133729	1.303827637	0.679525	-3.68E-05		19.35611		1.96E-03	4.28E-01

Fig. 5(A) tensile test results from UMT machine

4. Numerical results and discussion

4.1 Tensile test for dissimilar welded joint

The tensile test specimens were prepared according to the ASTM E8 standard. The detailed dimensions of the actual specimen are provided in Fig. 5(d). A dog-bone-shaped workpiece was cut using an EDM (Electrical Discharge Machining) process, which achieves highly accurate dimensions. The finished specimen is shown in Fig. 5(c). The tensile test was conducted using a Digital UTM (Universal Testing Machine) at a speed of 2 mm/min, as shown in Fig. 5(a). An extensometer was mounted on the welded specimen to record strain values with respect to the applied load. Upon completion of the test, the results were generated in an Excel file as shown in Fig. 5(A). The data included axial displacement (Column A), axial load (kN) in Column B, time in Column C, and strain in Column D for each sample. The yield strength was then calculated from the

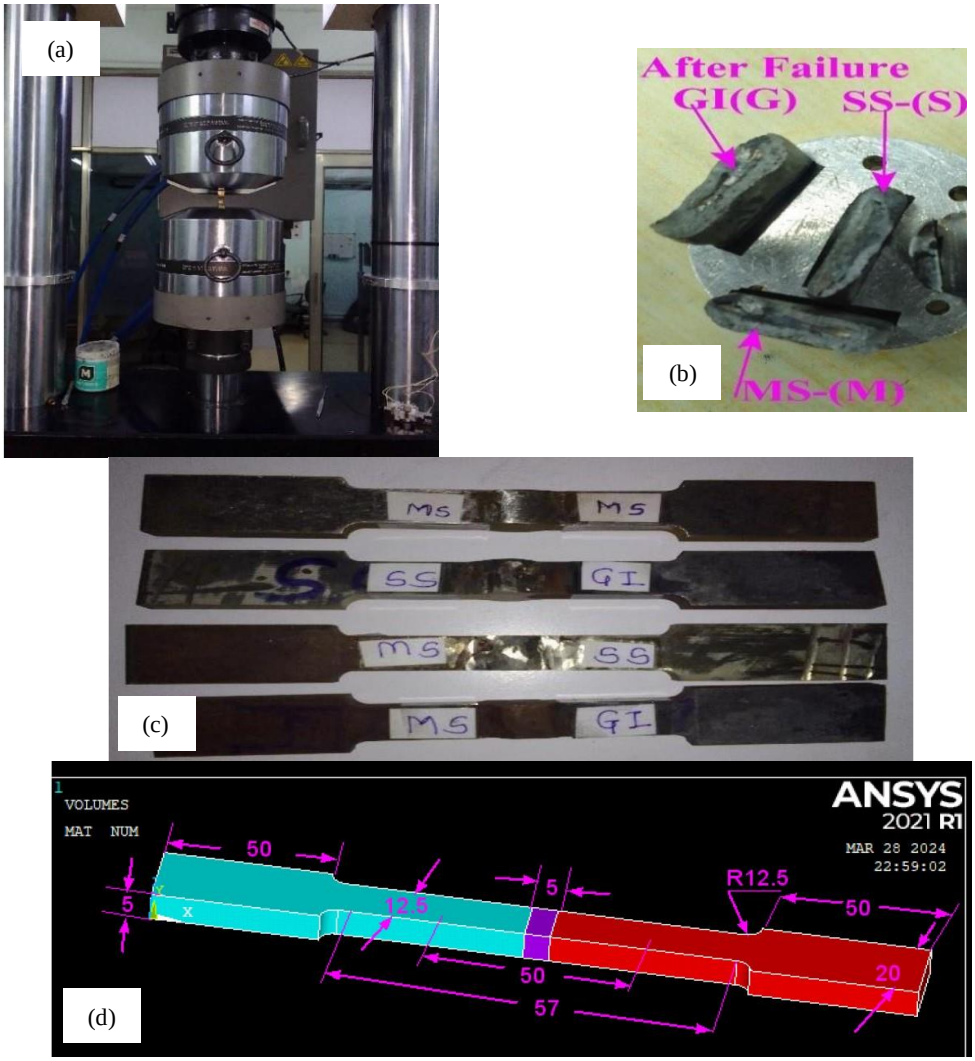

Fig. 5 Actual experimental set-up for Butt joint (a) Digital UTM (b) After failure different martials (c) dog bone shape specimen (d) Preparation of tensile specimens with detail dimension of ASTM -E8 slandered

experimental data using the following process: The yield strength was determined from the experimental data using the following procedure. First, the engineering stress (Column F) was calculated for each load value using the formula: Stress=[Load (Column B)×1000]/Area (67.36). A stress-strain graph was plotted using the data from Column D (strain) and Column F (stress). The modulus of elasticity (E), or Young's modulus, was determined as the slope of the linear elastic region of this stress-strain curve, with the value recorded in cell G8. An offset strain of 0.2% was applied (Column H=0.002). The corresponding offset stress (Column I) was then calculated as Offset Stress=Offset Strain (Column H)×Modulus of Elasticity (E), using the formula =H×(G8). The maximum load (in kN) was identified as the highest value in Column B, and the maximum displacement was the highest value in Column A. The ultimate tensile strength (UTS) was calculated as the maximum stress value in Column F. The offset stress-strain curve (using Columns H and I)

Table 1 Experimental evaluated mechanical properties of dissimilar welded joint

Mechanical properites	MS-MS	MS-SS	MS-GI	SS-GI
YS (MPa)	322	384	343	325
Load (KN)	35.378	35.713	34.807	27.498
Deformation (mm)	14.792	5.573	12.083	2.662
UTS (MPa)	509.259	526.587	489.178	408.225
Youngs Modulus (GPa)	204.340	171.243	234.481	218.497

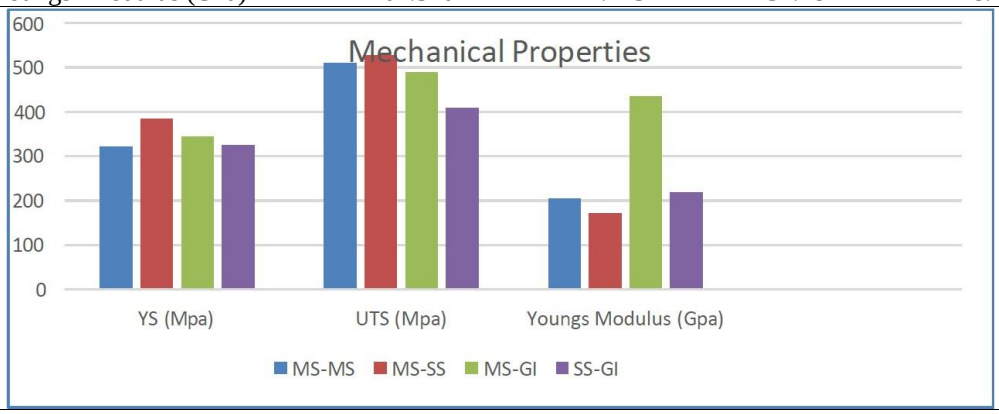

was plotted on the same graph as the axial stress-strain curve (using Columns D and F). The stress value at the intersection point of these two curves was identified as the yield strength (YS) of the sample, as per the 0.2% offset method. This procedure was applied to the MS-MS, MS-SS, MS-GI, and SS-GI dissimilar welded joints, and the resulting yield strength values are shown in Fig. 6 (a)-(d). The yield load was calculated as: Yield Load=Yield Strength (YS)×Cross-Sectional Area at the Failure Section. The mechanical properties of the dissimilar welded joints, obtained from the above procedure, are tabulated in Table 1. The results show that the MS-SS welded joint has the maximum yield strength, while the MS-MS joint has the minimum. This indicates that the MS-SS welded joint is significantly stronger under tensile load than the MS-MS joint. The MS-SS joint also demonstrated the highest load capacity, with a maximum of 35.71 kN. The experimental load-deformation curves for the MS-MS, MS-SS, MS-GI, and SS-GI joints are plotted in Figures 6(a-d), respectively. Fig. 6(e) compares the load capacity versus deformation for the different dissimilar welded joints. It is observed that the MS-SS joint sustains a larger load than the others. Consequently, the MS-SS welded joint is the most suitable for use in milk transport tanker structures.

4.2 FEM model validated with experimental data

A finite element model has been developed for the dissimilar welded joint subjected to a tensile load. The present analysis utilized the SOLID187 element with a mesh size of 5 mm. The entire model was discretized into 969 elements and 2045 nodes. The boundary conditions and the simulated FE model for the welded joint are presented in Fig. 7 (a)-(b). The detailed analysis and a step-by-step solution procedure for the ANSYS software are provided in Section 2. The material properties of the different metals are given in Table 2. The FEA model was simulated in ANSYS, and the results were compared with the experimental data for the different joint configurations, as shown in Table 3. It is observed that the ANSYS results are in close agreement with the experimental

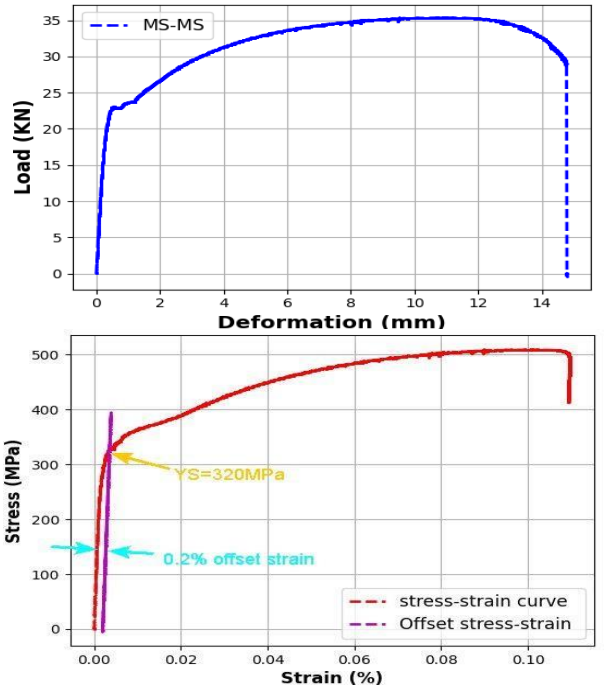

(a)

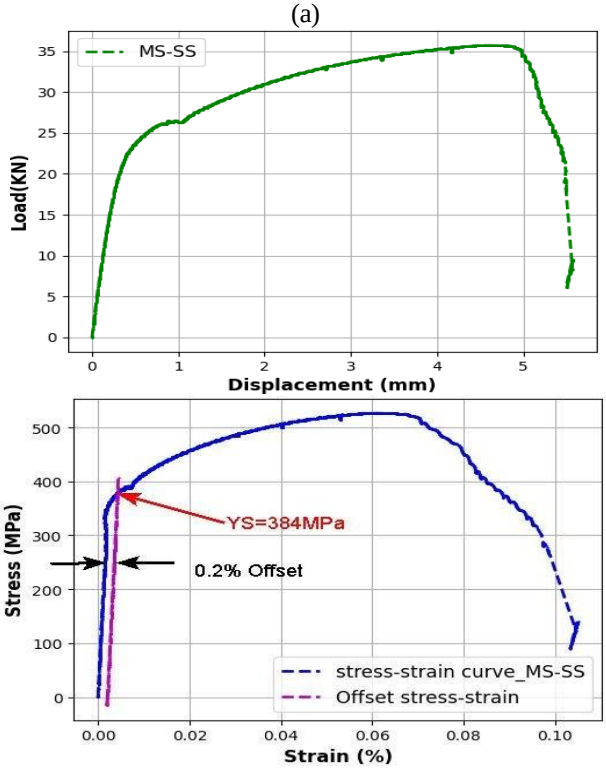

(b)

Fig. 6 Tensile test results plotted load against deformation and stress-strain curve for different welded joint (a) MS-MS (b) MS-SS (c) MS-GI (d) SS-GI (e) comparisons all model Load v/s deformation

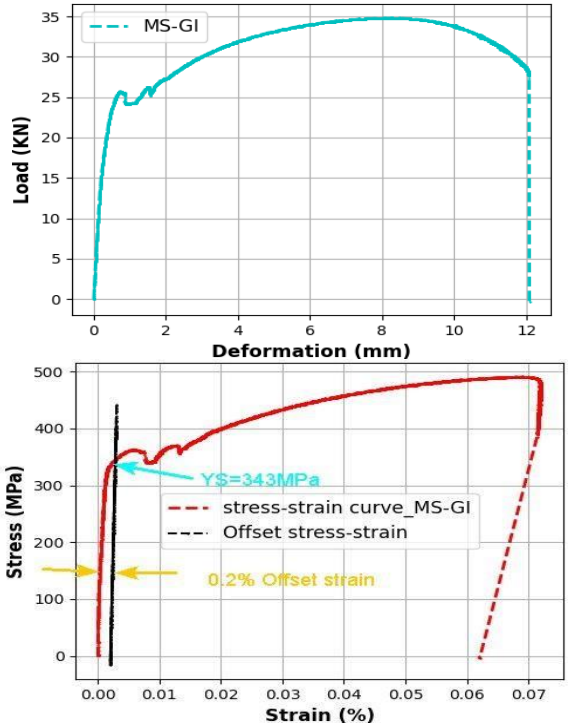

(c)

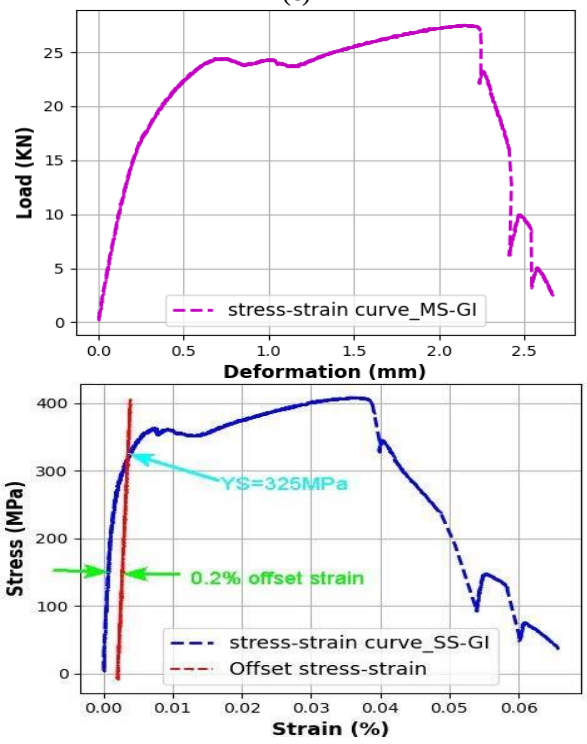

(d)

Fig. 6 Continued

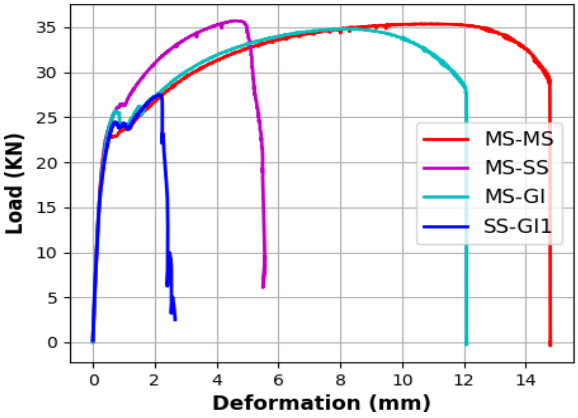

(e)

Fig. 6 Continued

Table 2 Material property for different material

	MS	SS	GI
Young Modulus (GPa)	207	190	196
Passion Ratio	0.3	0.28	0.25

Table 3 Compression FEM (ANSYS) results with experimental results for different cases

A] MS-MS welded joint subjected to tension loading			
Experimental results		ANSYS Results	
Load (KN)	Deformation (mm)	Load (KN)	Deformation (mm)
1.249551758	0.014039504	1.249551758	0.01547
5.838824219	0.066083427	5.838824219	0.06587
10.0206748	0.119049997	10.0206748	0.1120
15.00236914	0.197731861	15.00236914	0.1999
20.5759375	0.343662134	20.5759375	0.356875
25.21766602	1.521001686	25.21766602	1.523685
31.88513672	4.369005561	31.88513672	4.36874
35.05249219	8.757022209	35.05249219	8.74999
35.37559375	10.90998296	35.37559375	11.02548

results. Therefore, the proposed model demonstrates good correlation with the experimental data. The FEM model was used to analyze the effect of increasing load for the different joint models, while keeping all other parameters constant, as summarized in Table 4. The resulting principal stress and von Mises stress values for the respective loads are reported. Furthermore, the stress singularity was calculated using Eq. (12), and these values are also included in Table 4.

4.3 Failure analysis

The ANSYS results for the different models (MS-MS, MS-SS, MS-GI, SS-GI) are presented in Table 4. The failure criterion was then applied using Eqs. (26)-(27). The corresponding Python code

Table 3 Continued

B] MS-SS welded joint subjected to tension loading			
Experimental results		ANSYS Results	
Load (KN)	Deformation (mm)	Load (KN)	Deformation (mm)
1.294324	0.012804	1.294324	0.0112485
4.769192	0.05337	4.769192	0.04998
7.11628	0.08607	7.11628	0.087254
10.58286	0.134623	10.58286	0.129925
17.09387	0.244603	17.09387	0.24358
20.02743	0.314708	20.02743	0.302548
32.31369	2.425963	32.31369	2.9854
34.00536	3.162694	34.00536	3.25844
35.04959	3.849184	35.04959	3.82458
35.71229	4.593386	35.71229	4.60258
C] MS-GI welded joint subjected to tension loading			
Experimental results		ANSYS Results	
Load (KN)	Deformation (mm)	Load (KN)	Deformation (mm)
2.13566	0.023269	2.13566	0.022254
8.888131	0.106729	8.888131	0.11586
10.05596	0.124127	10.05596	0.124127
15.21183	0.206575	15.21183	0.19685
20.21231	0.354591	20.21231	0.34998
25.2762	0.648923	25.2762	0.648749
30.27676	3.088346	30.27676	2.9985
34.15674	6.252246	34.15674	6.02548
34.80038	8.345632	34.80038	7.99874
34.7607	8.493704	34.7607	8.87548
D] SS-GI welded joint subjected to tension loading			
Experimental results		ANSYS Results	
Load (KN)	Deformation (mm)	Load (KN)	Deformation (mm)
1.162532	0.010565	1.162532	0.0115894
5.041465	0.056954	5.041465	0.055689
10.02296	0.118951	10.02296	0.112584
13.23807	0.168888	13.23807	0.159985
17.39306	0.270227	17.39306	0.26985
20.25024	0.385541	20.25024	0.389578
24.41824	0.680527	24.41824	0.6802548
26.25086	1.678737	26.25086	1.668954
27.49443	2.136757	27.49443	2.148527
27.48954	2.150403	27.48954	2.165848

for the von Mises stress calculation is provided in Appendix-A. A von Mises failure stress envelope was plotted for the MS-MS joint using the ANSYS results and a yield strength (YS) of 320 MPa, from which the failure load was determined to be 21.55 KN. Similarly, for the MS-SS joint (YS=384

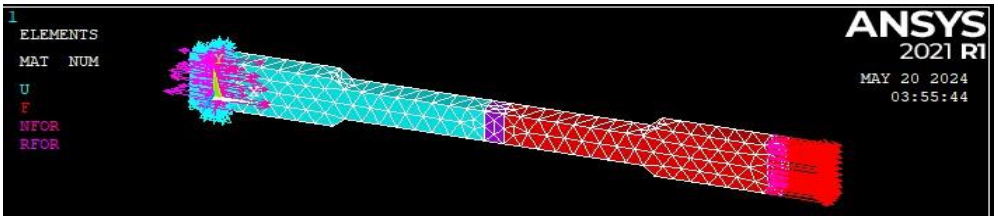

(a)

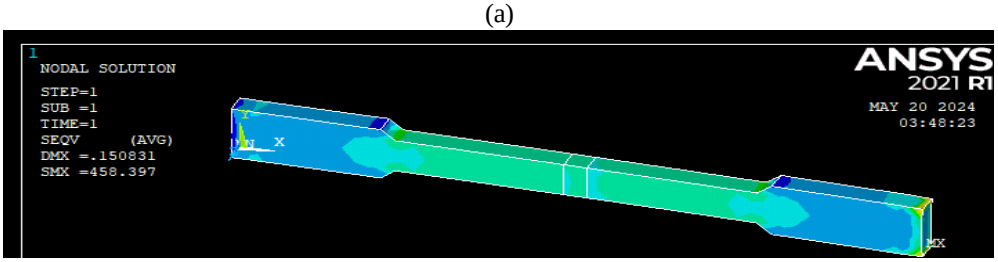

(b)

Fig. 7 ANSYS model for dissimilar welded joint subjected to tensile loading (a) Boundary condition (b) simulated model for welded joint

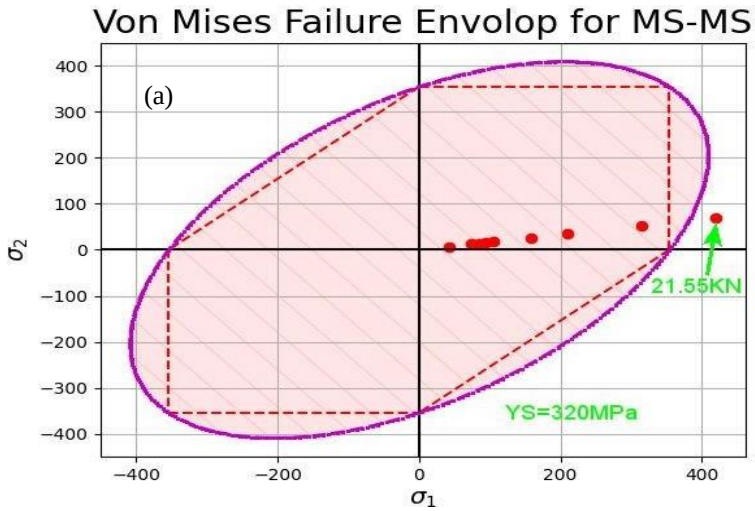

Fig. 8 Von misses failure stress envelope for dissimilar welded joint subjected to tensile load (a) MS-MS welded joint (b) MS-SS welded joint (c) MS-GI welded joint (d) SS-GI welded joints

MPa), the failure load was 26.048 KN. For the MS-GI model (YS=343 MPa), the failure load was 24.401 kN, and for the SS-GI joint (YS=325 MPa), it was 21.892 KN. The failure stress envelopes for all models are plotted in Fig. 8. A parametric study was conducted for the dissimilar metal welded joints. The variation in stress singularity with different loading conditions for all joint configurations is shown in Fig. 9. The results show that the stress singularity remains constant after a load of 4 KN for all models. This indicates that the stress state in all welded models stabilizes beyond the 4 KN load. An unstable model would require a refined mesh for accurate analysis. Fig. 10 shows the stress distribution along the length of the welded specimen. The maximum stress occurs at the center position compared to other locations, with the specific stress values at different points provided in

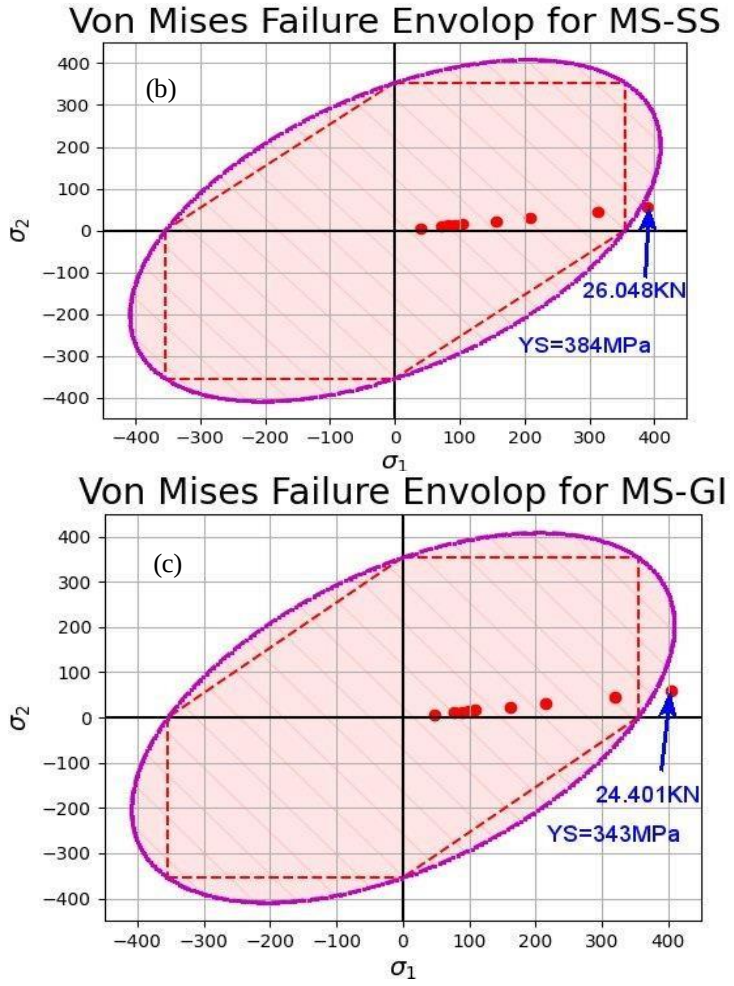

Fig. 8 Continued

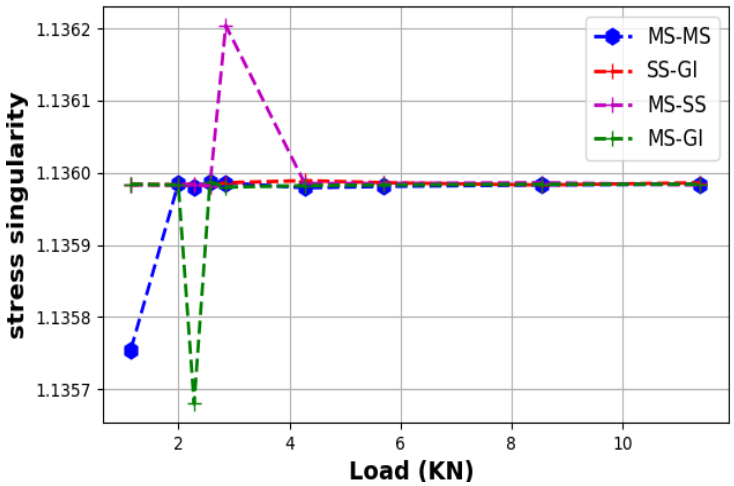

Fig. 9 Load V/s stress singularity for various dissimilar welded joints

Table 4 Dissimilar welded joint simulated results from ANSYS software for all models

Load (KN)	σ_1 (MPa)	σ_2 (MPa)	σ_{von} (MPa)	Stress singularity= $\frac{avon}{\sigma_1}$
MS-MS ; YS from Experimental=320 MPa				
1.5	42.0337	6.97581	47.74	1.135755
2.5	73.559	12.2077	83.5619	1.135985
5.5	84.0675	13.9516	95.499	1.13598
10.5	94.5759	15.6956	107.437	1.135987
15.68	105.084	17.4395	119.374	1.135986
17.258	157.627	26.1593	179.061	1.135979
18.35	210.169	34.8791	238.748	1.135981
19.568	315.253	52.3186	358.122	1.135983
21.55	420.337	69.7581	477.496	1.135984
MS-SS; YS from Experimental=384 MPa				
2	46.2371	6.68468	52.5246	1.135984
3.5	77.7624	11.2424	88.3368	1.135983
6.5	86.1692	12.4578	97.8868	1.135984
8	92.4742	13.3694	105.049	1.135982
12.5	105.084	17.4395	119.374	1.135986
18.5	151.321	21.8771	171.899	1.135989
22.568	199.66	28.8657	226.811	1.135986
24.589	294.236	42.5389	334.247	1.135983
26.0458	399.32	57.7314	453.622	1.135986
MS-GI; YS from Experimental=343 MPa				
1.5	39.9321	5.77314	45.3622	1.135983
3.5	71.4574	10.3309	81.1744	1.135983
5.5	81.9658	11.8501	93.1118	1.135984
9.58	92.4742	13.3694	105.049	1.135982
15.54	102.963	14.8886	116.987	1.136204
18.59	155.525	22.4848	176.674	1.135985
22.58	208.067	30.0811	236.361	1.135985
23.658	313.151	45.2735	355.735	1.135986
24.401	388.812	56.2121	441.684	1.135983
SS-GI; YS from Experimental=325 MPa				
1.14	48.3388	6.98853	54.9121	1.135984
5.5	77.7624	11.2424	88.3368	1.135983
7.78	88.2709	12.7617	100.2475	1.13568
12.548	98.7793	14.2809	112.212	1.135987
15.368	109.288	15.8002	124.149	1.13598
18.258	161.83	23.3964	183.836	1.135982
19.356	214.372	30.9926	243.523	1.135983
20.589	319.456	46.1851	362.897	1.135984

Table 5. It is observed that the maximum stress develops in the dog-bone shaped specimen. This is because the cross-sectional area is smallest at the center, leading to a higher stress concentration at that position. Fig. 11 shows the effect of weld thickness on the strength of the dissimilar welded

Table 5 The different stress value for all dissimilar welded joint with changing length in X-Direction

Length	SS-GI			MS-SS			MS-GI		
	σ_1	σ_{von}	σ_2	σ_1	σ_{von}	σ_2	σ_1	σ_{von}	σ_2
3	115	24.6479	8.6485	94.8534	112.6985	24.6479	29.1787	115.386	28.428
6	112.961	115.177	114.184	110.138	109.461	115.177	115.224	119.158	118.725
9	113.423	122.7935	112.419	119.52	132.5897	122.7935	124.0865	149.292	137.516
12	116.839	141.6541	136.09	137.929	166.6584	141.6541	143.1459	181.894	172.9865
15	130.886	178.6587	165.7365	173.945	175.0265	178.6587	180.5874	181.891	180.5894
18	251.841	178.1574	178.0658	173.4503	178.2154	178.1574	180.421	184.84	179.998
21	184.712	178.059	178.078	178.083	178.8059	178.059	185.6223	184.558	112.8748
24	182.712	178.2265	183.037	179.33	174.2548	178.2265	181.139	187.124	180.2548
27	181	188.8925	184.977	179.883	144.212	188.8925	180.1245	180.8359	186.3985
30	183.219	178.254	186.06	174.559	137.4568	178.254	180.029	179.9857	185.9875
33	186.028	178.1358	178.955	173.43	117.9587	178.1358	145.3658	180.5978	179.9857
36	182.04	156.448	178.109	175.43	115.2548	156.448	127.07	172.7895	184.8578
39	170.936	150.5894	178.032	147.087	105.75	150.5894	116.795	142.346	180.5987
42	150.31	115.3025	179.7895	112.537	96.5487	115.3025	111.652	116.97	172.7368
45	121.256	112.4587	148.145	107.584	81.6598	112.4587	94.8354	97.33	142.3658
50	91.25	113.658	134.938	91.405	27.2359	113.658	72.3568	85.3587	113.0985
55	90.325	105.236	113.874	66.987	17.359	105.236	70.2658	77.685	113.173
57	85.35	89.256	108.587	65.365	17.8497	89.256	66.3258	72.3658	100.235

joint. The results demonstrate that increasing the weld thickness leads to a decrease in stress. This is because a larger weld thickness provides a greater cross-sectional area, distributing the load more effectively and reducing stress concentration. Therefore, the structural strength improves with increased weld thickness.

5. Fractography study

This section focuses on the SEM, DSE, and EBSD analysis of the different failure surfaces, namely the MS failure surface, GI failure surface, and SS failure surface, as shown in Fig. 5(b). A detailed explanation is provided below.

MS material failure analysis

The surface characterization of the MS material failure indicates an increased number of obstacles, making crack propagation more challenging, as shown in Fig. 11 (a)-(c). The surface of the welded MS steel specimens experienced plastic deformation during the tensile test, resulting in grain refinement and a reinforced structure. Fig. 12(a) shows a micrograph of the failure surface at the interface between the base metal and the weld material, where the weld material exhibits ductile failure. Fig. 12(b) shows a mixed-mode failure (ductile and brittle) with the presence of large dimples. A few dislocations proliferated and transitioned into a larger number within this strengthened interface zone, enhancing the tensile strength. In Fig. 12(c), the microscopic cracking mechanism that propagated at the welded location is visible. A tearing ridge pattern and brittle

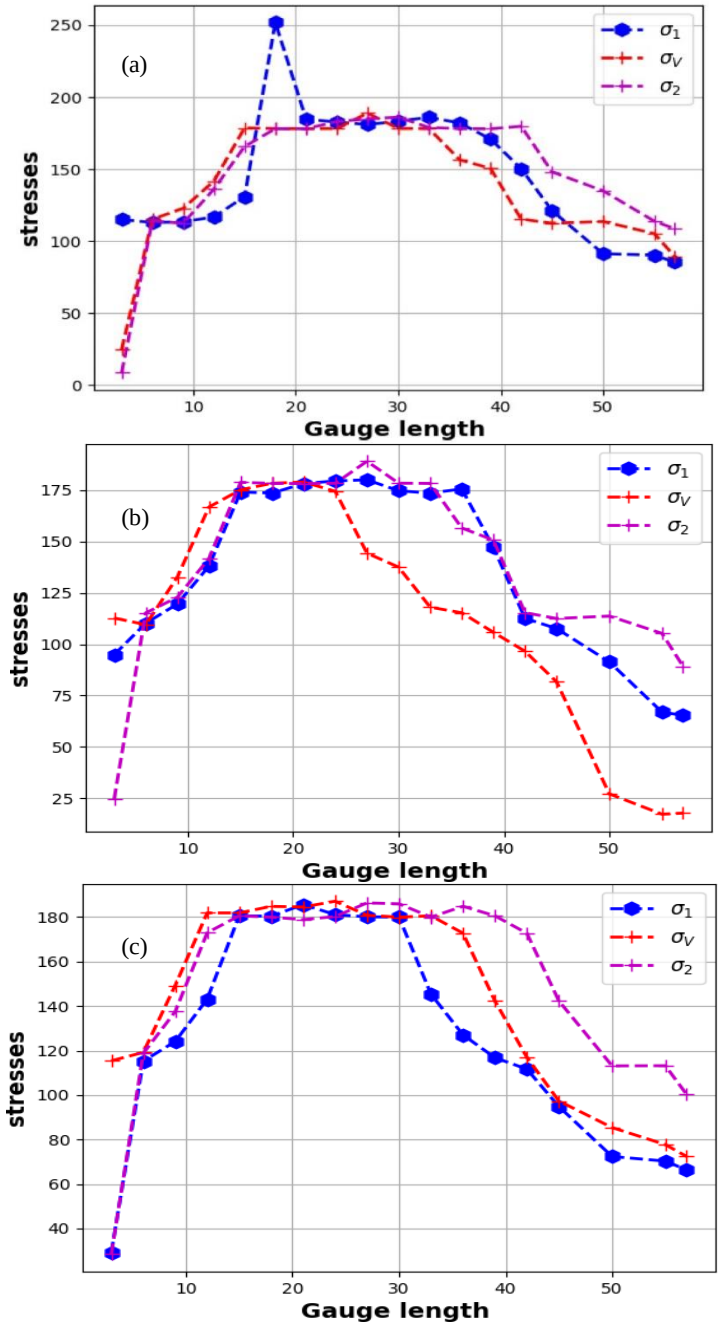

Fig. 10 Stresses (Principle stress 1, Principle stress 2 &von misses stress) distribution over length of dissimilar welded specimen (a) SS-GI welded joint (b) MS-SS welded specimen (c) MS-GI welded joint specimen

failure of the MS material are also observed. Fig. 12(e) indicates that the material's dislocation structure was prone to slippage. Under external tensile loads, the material experienced both elastic and plastic deformation at the grain boundary interface region. Fig. 12 (f)-(g) show the Inverse Pole

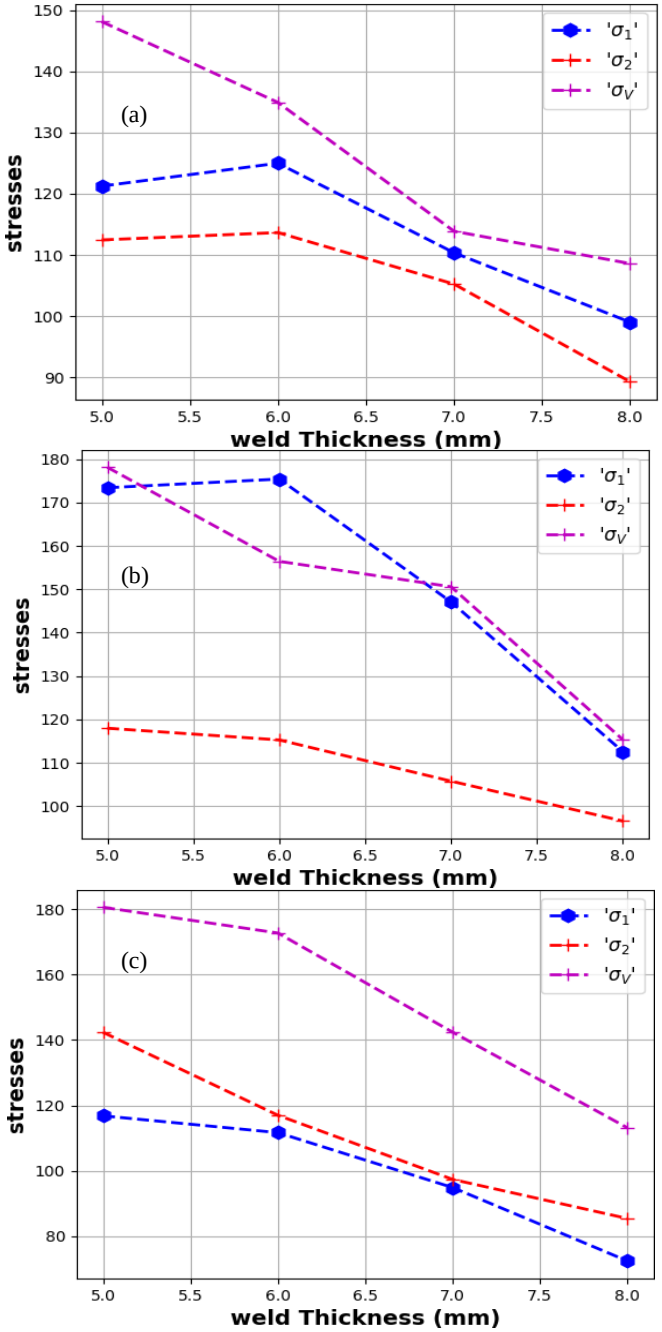

Fig. 11 the stresses values for different weld thickness (a) MS-SS welded joint (b) MS-GI welded joint (c) SS-GI welded joint

Figure (IPF) maps and phase diagram of the tensile-loaded fracture surfaces for the MS samples, confirming that all welds failed in their central regions. Fig. 12 (h)-(i) present the image quality map and grain boundary analysis at the interface surface of the welded joint under axial loading. Kernel

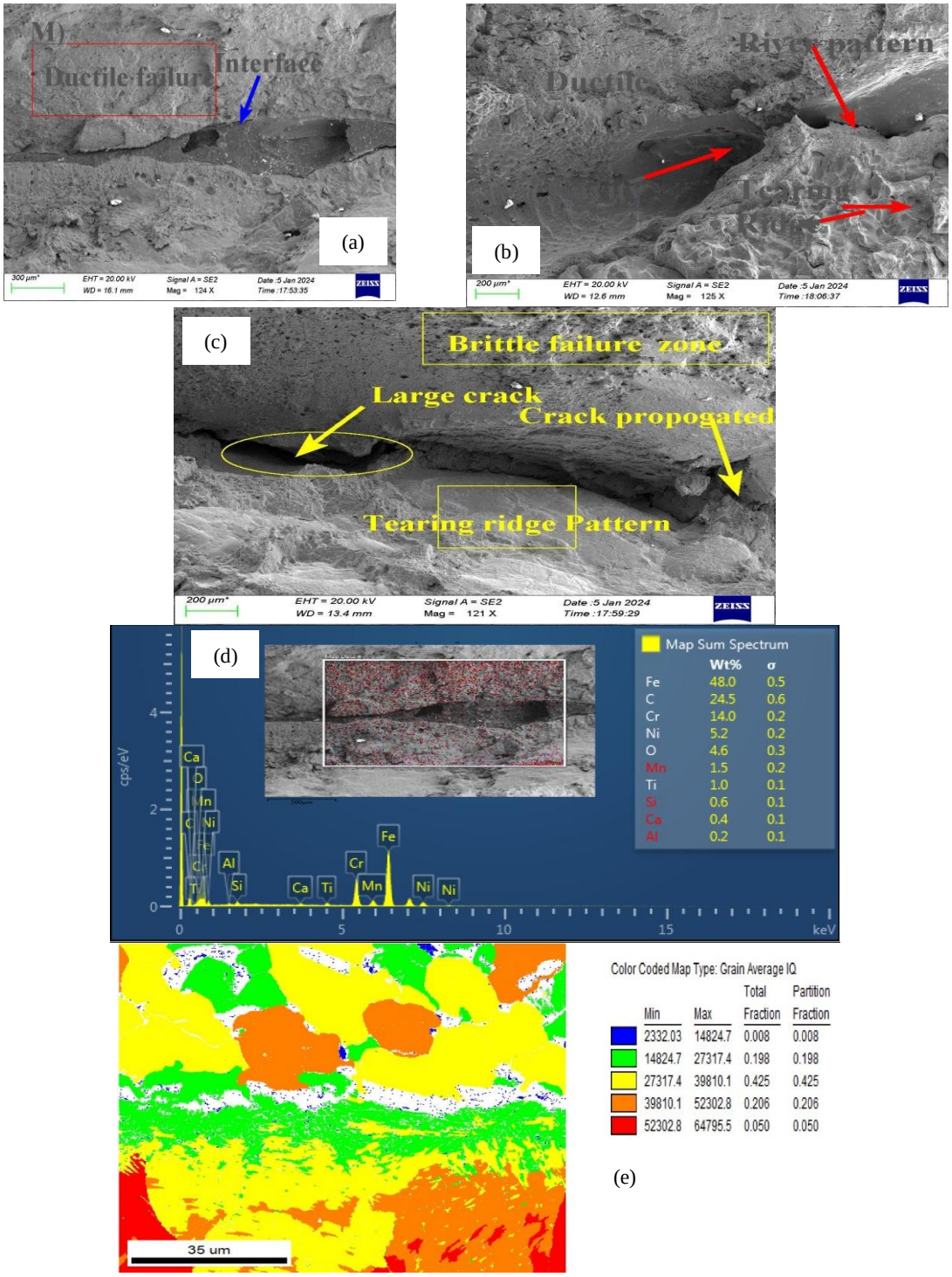

Fig. 12 SEM-EDS-EBSD analysis for failure of MS surface (a) SEM image at interface (b) & (c) SEM image (d) EDS chemical composition; EBSD images (e) Grain boundary for interface welded and base metal (f) IPF map (g) Phase diagram (h) QI interface welded joint and base metal (i) Grain boundary (j) KAM

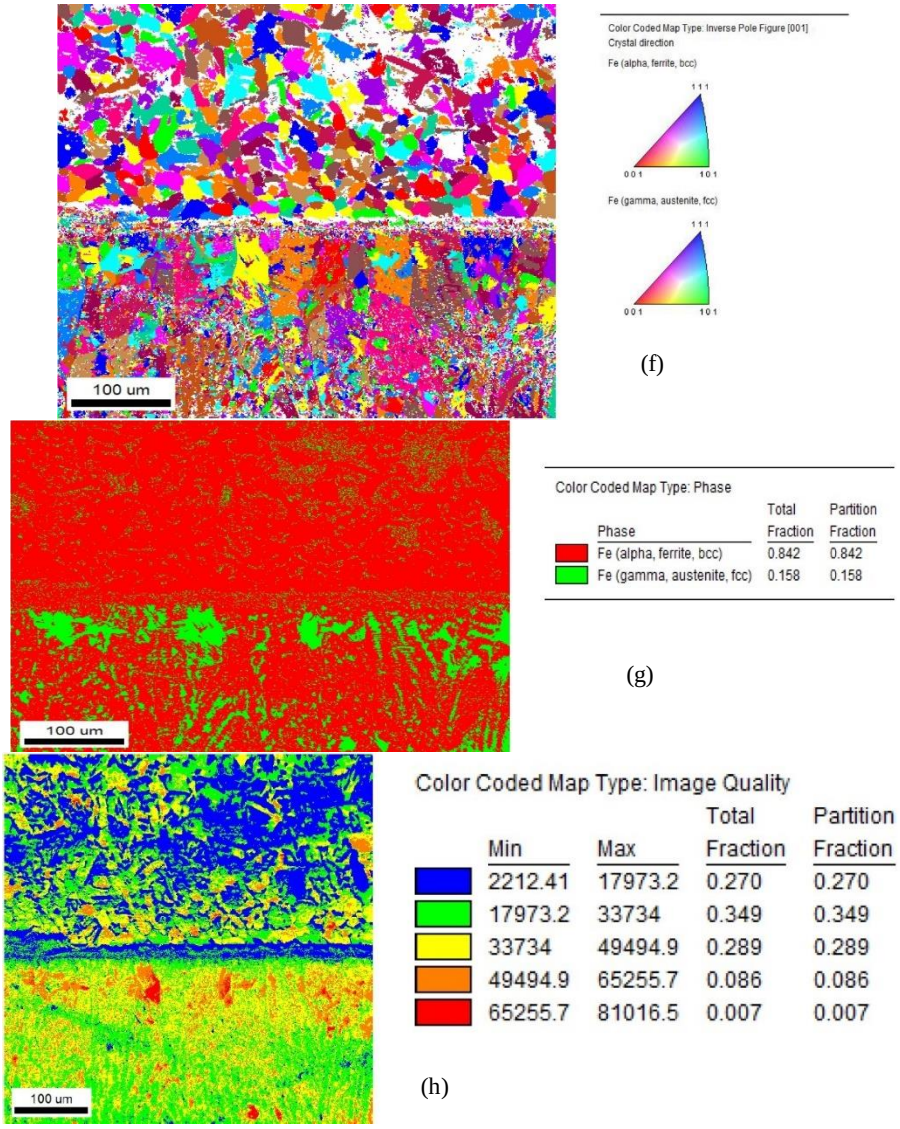

Fig. 12 Continued

Average Misorientation (KAM) maps, shown in Fig. 12(j), provide a microscopic analysis of the tensile action on the failure surfaces. It was determined that grain refinement, along with the propagation and motion of dislocations, were the primary factors governing the tensile performance of the dissimilar welded joint.

5.1 GI material failure analysis

Fig. 13(a) shows the GI failure surface after dissimilar material failure. The dislocation density increases significantly and exhibits a ramp distribution along the depth. A maximum concentration of spherical carbides and large cracks was observed in this region. The GI surface was examined at

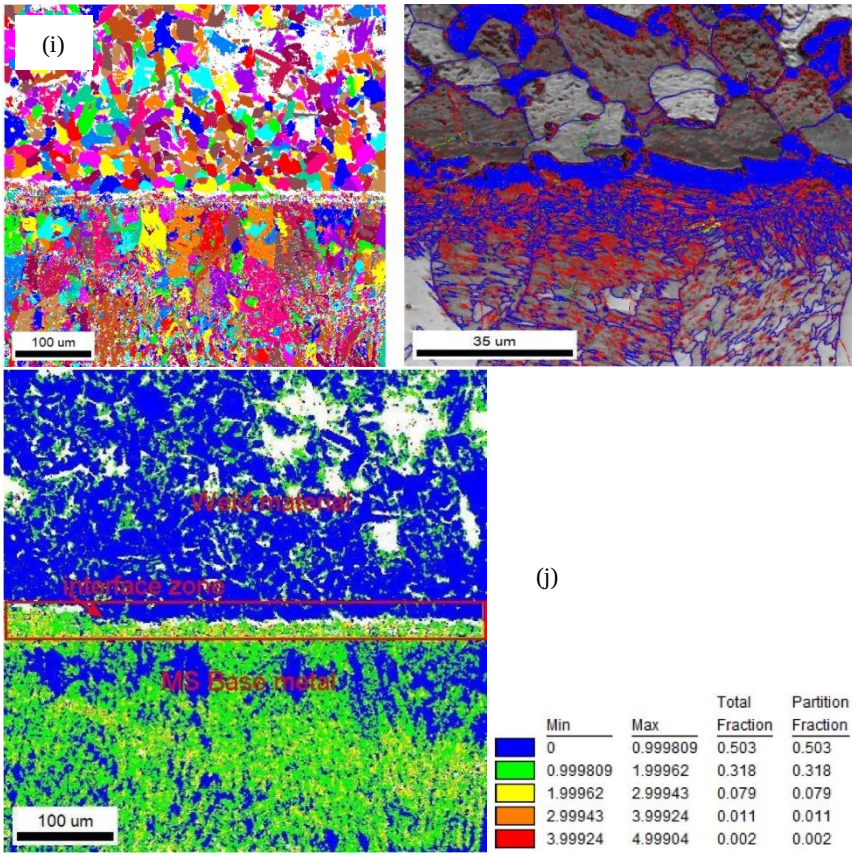

Fig. 12 Continued

different locations, as shown in Fig. 13(b), revealing a large number of dimples and a fish-net pattern. This morphology, along with the presence of large cracks, is indicative of ductile failure. EDS analysis was carried out on the GI failure surface. Fig. 13(c) shows the chemical composition, which includes Fe (60.4 wt.%), Si (0.6 wt.%), C (12.1 wt.%), and Ni (3.1 wt.%). The high carbon percentage at the welded location identifies this zone as a carburization zone. Fig. 13 (d) and (f) show dislocated grain boundaries on the GI failure surface. These defects resulted from rapid localized heating and cooling during welding, which generated substantial residual tensile stress. The Inverse Pole Figure (IPF) and Phase maps are shown in Fig. 13 (e) and (h), respectively. Fig. 13(g) depicts the Kernel Average Misorientation (KAM) map. The KAM size is closely related to the material's dislocation density. Increased KAM values correlate with higher hardness, strength, and deformation resistance. When combined with external loading, the residual tensile stress exacerbates the local stress within the joint, initiating cracks and reducing the joint's integrity. After processing, the samples experienced penetrating plastic deformation, which contributed to the development of residual tensile stresses.

5.2 SS material failure analysis via SEM, EDS, and EBSD

SEM, EDS, and EBSD analyses were conducted on the failure surface of the SS material. Fig.

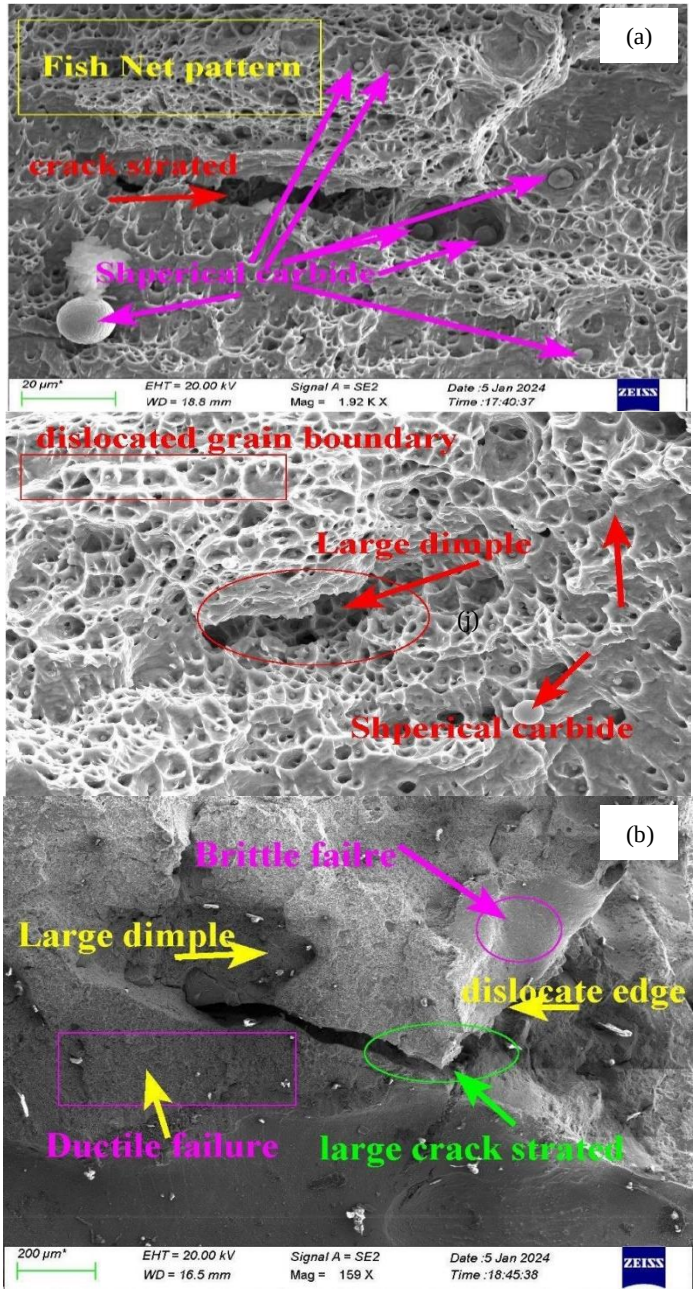

Fig. 13 SEM-DSE-EBSD analysis image for GI material failure surface (a) & (b) SEM image (c) DSE image and EBSD image (d) IPF map (e) Grain boundary (f) KAM Map (g) Phase diagram for GI failure surface (h) Average GB

14 (a) and (b) show that the crack origin propagates deeper into the specimen. The crack experiences tensile forces during propagation, evidenced by large cracks and a river pattern. The continuous opening and closing of the crack edges form small, smooth surfaces at the crack initiation point.

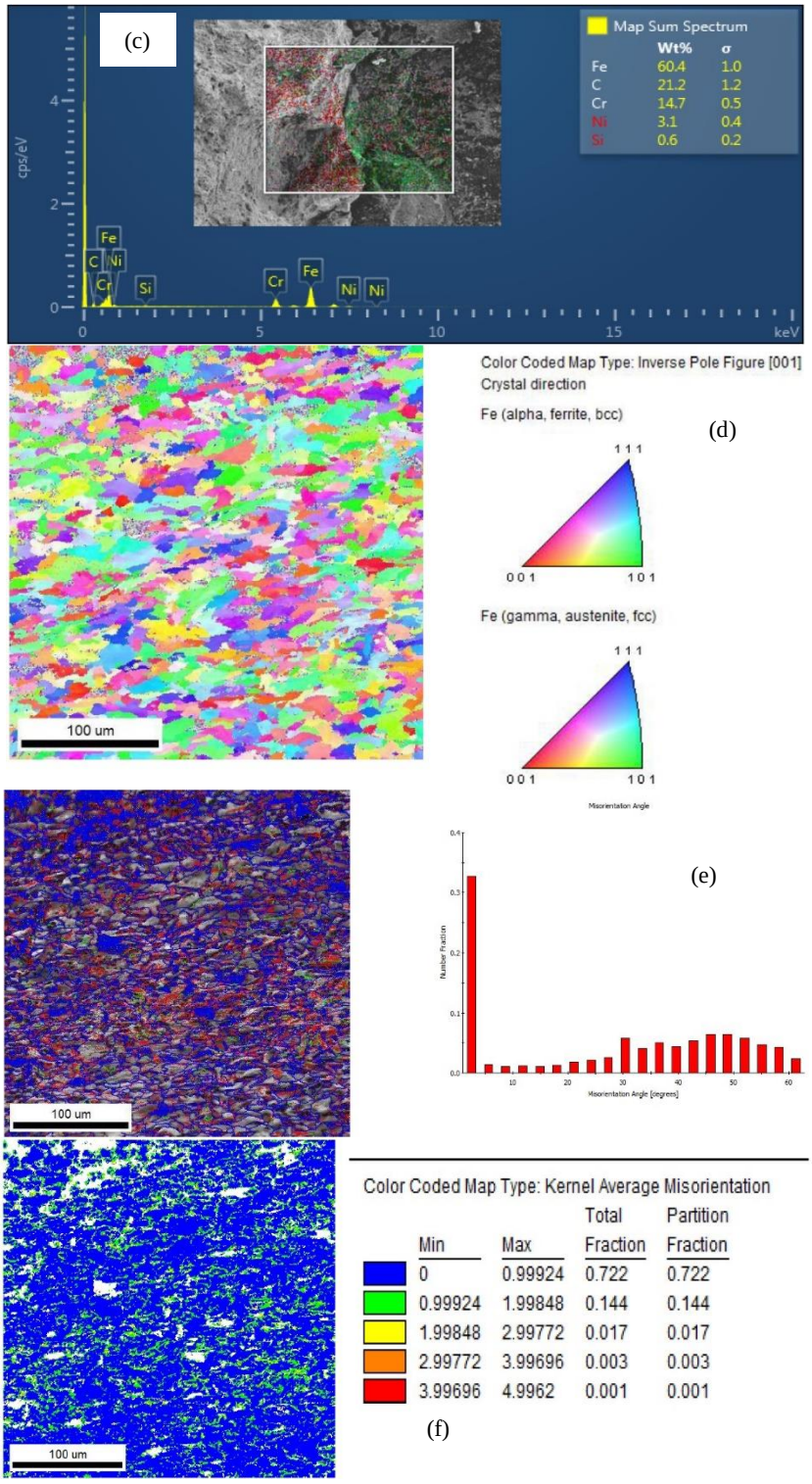

Fig. 13 Continued

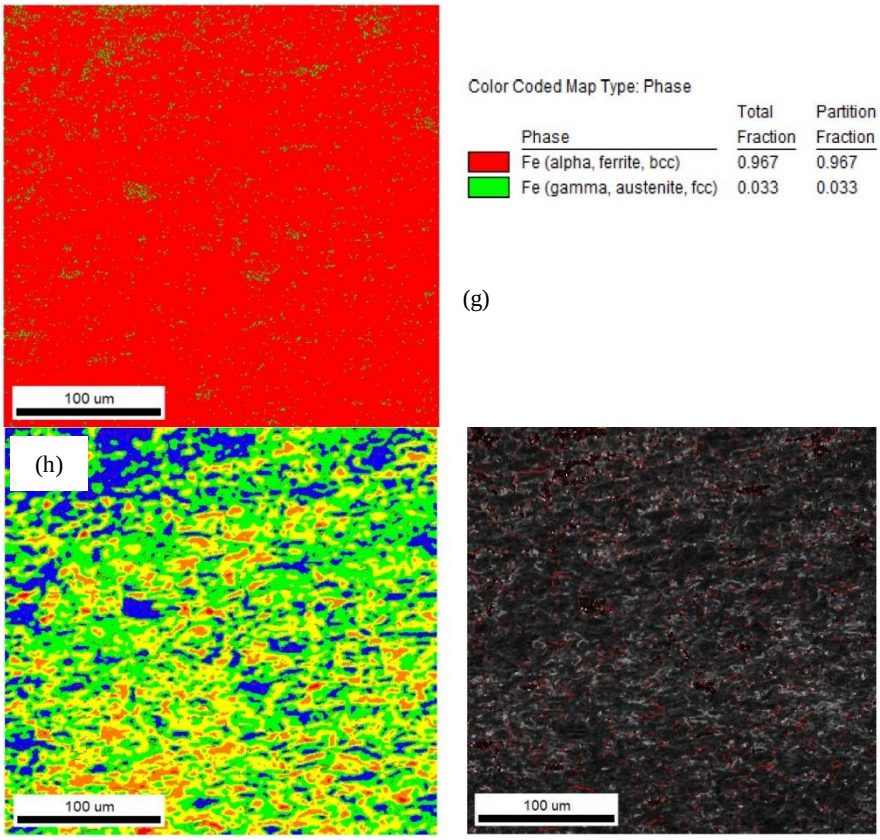

Fig. 13 Continued

Furthermore, Fig. 14(c) demonstrates the crack propagation path, where some inclusion particles exhibited a pseudo-cleavage, step-like pattern, indicating a mixed-mode failure (both ductile and brittle). The chemical composition of the SS failure surface, determined by EDS, is reported in Fig. 14(d). The weight percentages are: Fe=33.4%, C=31.1%, Ti=14.1%, Mn=3.6%, Ni=3%, and Si=2.1%. The presence of Ti and Mn, which are good corrosion-resistant components, along with the very limited plastic deformation, suggests a predominantly brittle failure. The EBSD analysis of the tensile failure at the welded location is presented in Fig. 14 (e)-(k). The grain boundary orientations and grain boundary (GB) rotation angles are shown in Fig. 14 (e)-(f) and (j)-(k). As a crack propagated, it often traversed grain boundaries. However, when the crack tip reached a boundary, it encountered resistance, leading to a change in direction. Grain refinement occurred on the SS failure surface, increasing the number of grains and grain boundaries, which impeded crack propagation. Fig. 14(g) depicts the Kernel Average Misorientation (KAM) map for the SS material failure surface. The Inverse Pole Figure (IPF) and phase image are shown in Fig. 14 (h) and (i), respectively. The dimple sizes on the SS failure sample were relatively uniform and primarily equiaxed, indicating homogeneous plastic deformation. This suggests that the stable tensile crack expansion was consistent during the stable propagation stage.

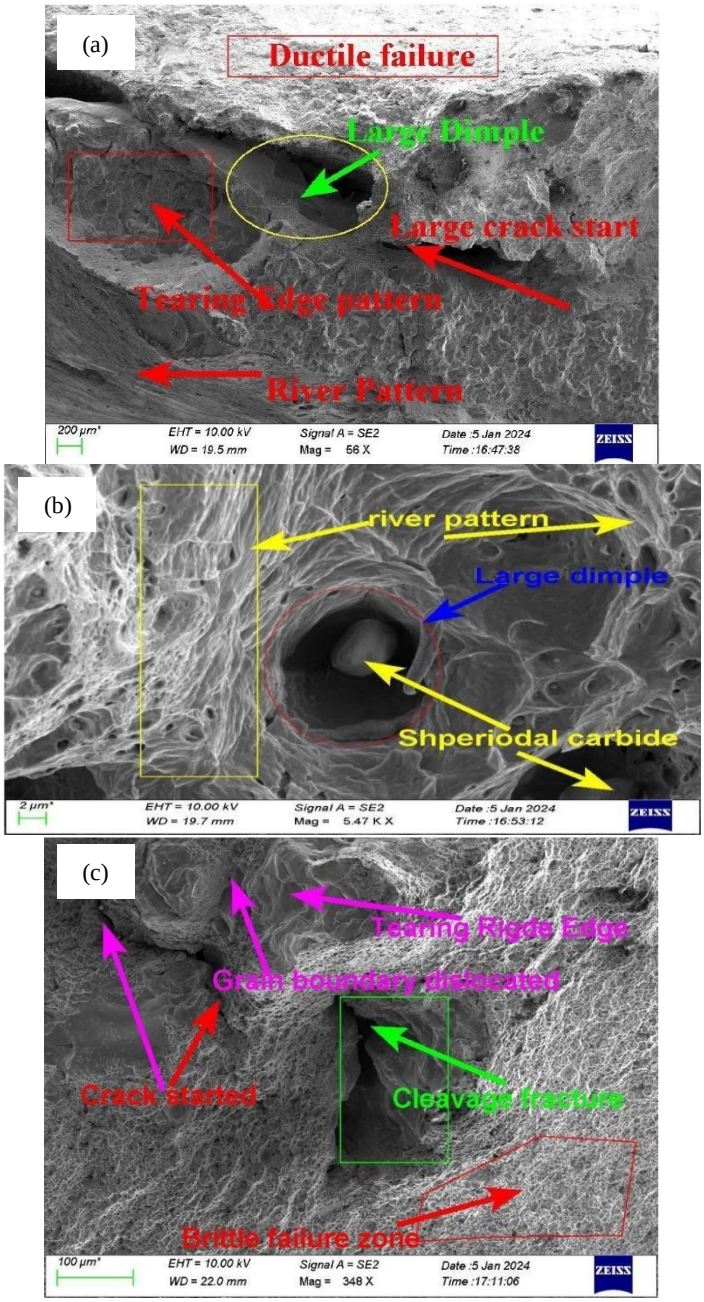

Fig. 14 Fractography analysis for SS material failure surface (a)-(c) SEM (d)-EDS (e) GB-rotation angle (f) Grain Boundary structure (g) KAM (h) IPF (i) Phase diagram (j) Grain size (k) EBSD

6 Conclusions

Dissimilar welded joints of SS304L, EN24T, and GI materials were tensile tested to evaluate their yield strength and load capacity. The microstructure and grain boundaries of the different

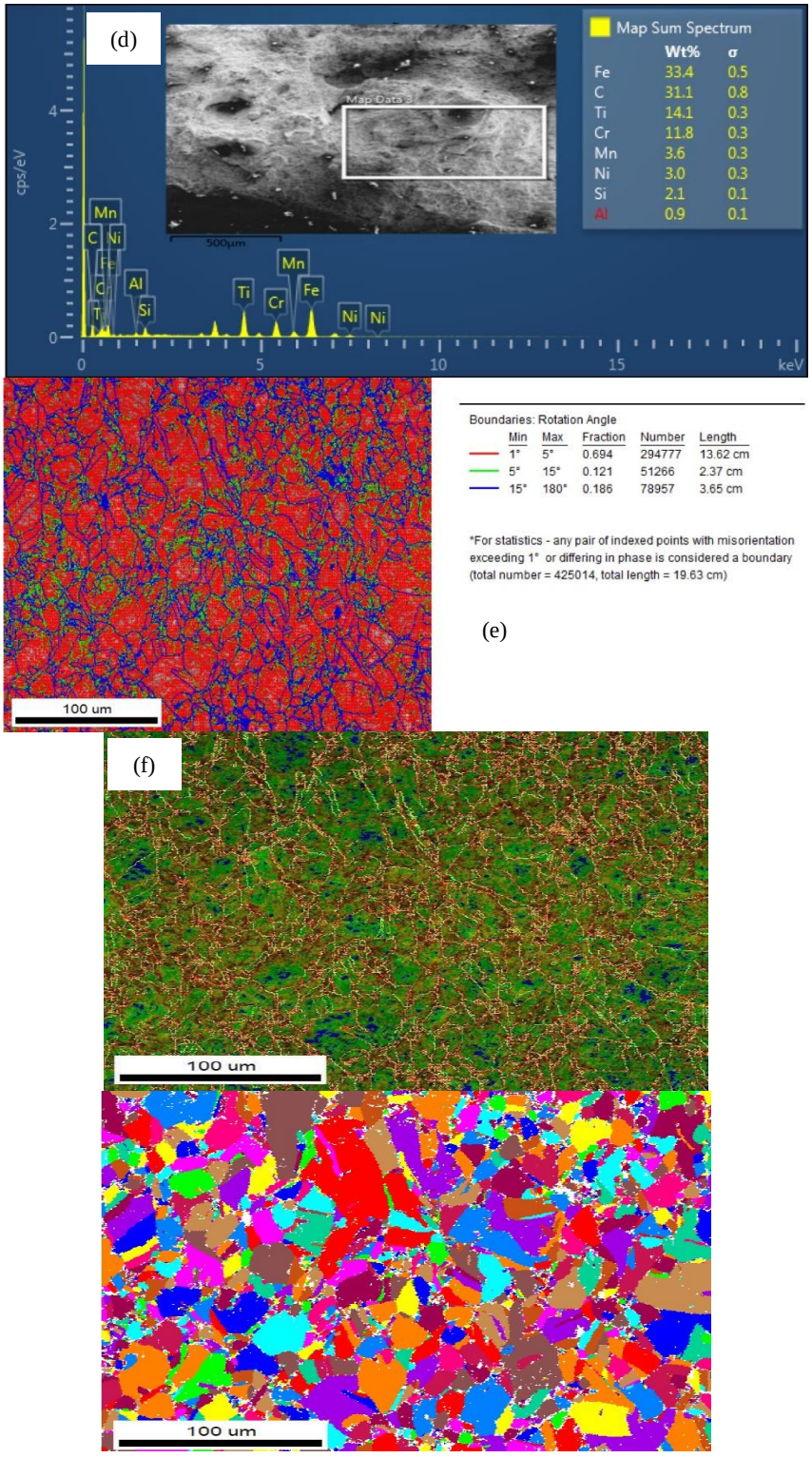

Fig. 14 Continued

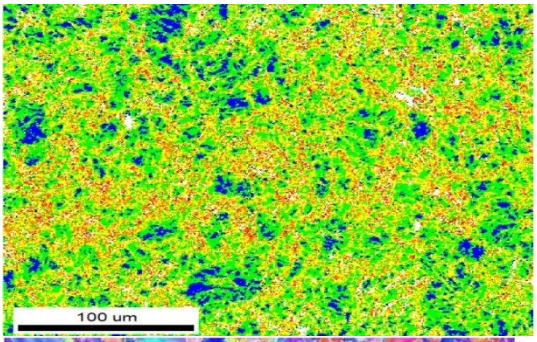

(g)

Color Coded Map Type: Kernel Average Misorientation

	Min	Max	Total Fraction	Partition Fraction
	0.167632	1.13408	0.088	0.088
	1.13408	2.10053	0.383	0.383
	2.10053	3.06697	0.318	0.318
	3.06697	4.03342	0.123	0.123
	4.03342	4.99987	0.024	0.024

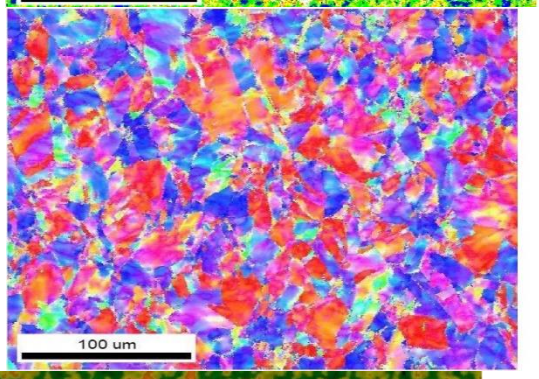

Color Coded Map Type: Inverse Pole Figure [001] Crystal direction

Fe (alpha, ferrite, bcc)

(h)

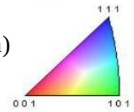

Fe (gamma, austenite, fcc)

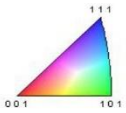

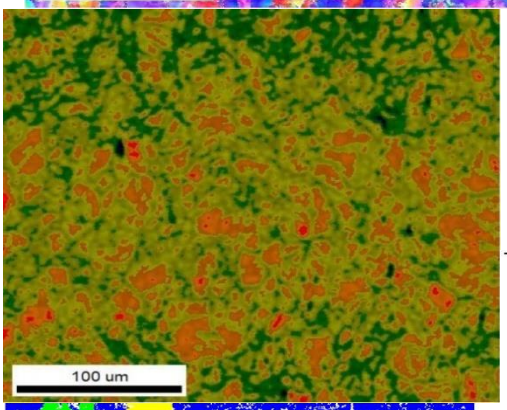

(i)

Color Coded Map Type: Phase

	Phase	Total Fraction	Partition Fraction
	Fe (alpha, ferrite, bcc)	0.031	0.031
	Fe (gamma, austenite, fcc)	0.969	0.969

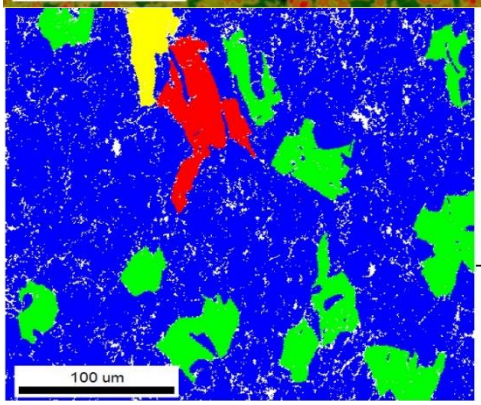

Color Coded Map Type: Grain Size (number of points)

	Min	Max	Total Fraction	Partition Fraction
	2	1112.4	0.745	0.745
	1112.4	2222.8	0.141	0.141
	2222.8	3333.2	0.016	0.016
	3333.2	4443.6	0.000	0.000
	4443.6	5554	0.034	0.034

(j)

Fig. 14 Continued

failure surfaces were thoroughly examined using Scanning Electron Microscopy (SEM) and Electron Backscatter Diffraction (EBSD). The mechanical properties of MS-MS, MS-SS, MS-GI, and SS-GI welded joints were determined through tensile tests on a Universal Testing Machine (UTM). Based on the findings, the MS-SS welded joint is concluded to be the most suitable for application in milk transport tanker structures. A Finite Element Method (FEM) model was developed in ANSYS software to simulate the behavior of the dissimilar welded joints under tensile loading. The results are summarized as follows:

1) An increase in weld thickness was found to decrease the stress value. This is attributed to the larger cross-sectional area, which reduces stress concentration, thereby resulting in a stronger weld structure.

2) The stress distribution along the length of the welded specimen was analyzed. The maximum stress was observed at the center, which is a direct result of the dog-bone geometry having its smallest cross-sectional area at that position.

During plastic deformation, the strengthening phases within the dissimilar weld joint interact with the microstructure, impeding the motion of dislocations. Furthermore, the material's residual tensile stress helps to suppress the formation of micropores at grain boundaries. This mechanism effectively slows the initiation of cracks and plays a vital role in mitigating microcracking.

Acknowledgement

The authors are extremely thankful to sophisticated analytical Instrument facility laboratory of Indian Institute of Technology Bombay (IIT-B), AMTF lab for providing the digital UTM and MMMF lab for preforming SEM-EDS-EBSD analysis facility assistance in this work.

References

ASTM International, Standard Test Methods for Tension Testing of Metallic Materials, 100 Barr Harbor Drive, PO Box C700, West Conshohocken, PA 19428-2959. United States.

Baskaya, U., Uzun, R., Atapek, S.H., Kılıc, Y. and Polat, S. (2024), "Effect of coating type on electrode degradation and its life in resistance spot welding of a low carbon steel", *Eng. Fail. Anal.*, **157**, 107879. https://doi.org/10.1016/j.engfailanal.2023.107879.

Bouchouicha, B., Tirenifi, M. and Bensari, A. (2019), "Numerical comparison of cruciform weld and butt weld simulation and a study of fracture mechanics on two types of welds", *Fract. Struct. Integr.*, **13**(48), 357-369. https://doi.org/10.3221/IGF-ESIS.48.34.

Chuaiphan, W., Kaewsakul, N. and Nansaarng, S. (2024), "Roles of hydrogen in shielding gas for compensate heat input on dissimilar joints of stainless steel series 200 between AISI 201LN and 214 by GTAW", *J. Alloy. Metal. Syst.*, **5**, 100052. https://doi.org/10.1016/j.jalmes.2023.100052.

Feizollahi, V. and Moghadam, A.H. (2024), "The study investigates the effects of tool pin length, rotation speed, and dwell time on the microstructure and tensile strength of dissimilar joints between low-carbon galvanized steel and aluminum T6-6061 through friction stir spot welding", *Eng. Fail. Anal.*, **157**, 107925. https://doi.org/10.1016/j.engfailanal.2023.107925.

Khater, N.S., El-Boghdadi, M.H. and Yossef, N.M. (2024), "Elastic distortional buckling of cold-formed steel Z-Beams with stiffened holes using reduced thickness", *Steel Compos. Struct.*, **51**(3), 225-241. https://doi.org/10.12989/scs.2024.51.3.225.

Koubova, L. (2024), "Solution of yielding steel arch supports used in mining", *Steel Compos. Struct.*, **51**(5), 575-586. https://doi.org/10.12989/scs.2024.51.5.575.

Kyaw, P.M., Osawa, N., Tanaka, S. and Gadallah, R. (2023), "Influence coefficient-based fracture parameter modification factor in a cracked T-butt welded joint", *Theor. Appl. Fract. Mech.*, **123**, 103678. https://doi.org/10.1016/j.tafmec.2022.103678.

Langari, J., Aliakbari, K. and Kolahan, F. (2023), "Fatigue life simulation of AA7075-T651 FSW joints using experimental data", *Eng. Fail. Anal.*, **154**, 107690. https://doi.org/10.1016/j.engfailanal.2023.107690.

Liu, M., Huang, S., Liu, Z. and Du, C. (2024), "Investigations on the passive and pitting behaviors of the multiphase stainless steel in chlorine atmosphere", *J. Mater. Res. Technol.*, **28**, 3365-3375. https://doi.org/10.1016/j.jmrt.2023.12.243.

Matuszewski, M. (2019), "Modeling of 3D temperature field in butt welded joint of 6060 alloy sheets using the ANSYS program", *IOP Conf. Ser., Mater. Sci. Eng.*, **659**, 012034. https://doi.org/10.1088/1757-899X/659/1/012034.

Mikolášek, D., Krejsa, M., Brožovský, J., Pařenica, P. and Lehner, P. (2017). "Numerical and experimental analysis of welds in steel structural element", *Zeszyty Naukowe Politechniki Częstochowskiej. Budownictwo*, 219-230. https://doi.org/10.17512/znb.2017.1.22.

Okada, H., Koya, H., Kawai, H., Li, Y. and Osakabe, K. (2016), "Computations of stress intensity factors for semi-elliptical cracks with high aspect ratios by using the tetrahedral finite element", *Eng. Fract. Mech.*, **158**, 144-166. https://doi.org/10.1016/j.engfracmech.2016.02.049.

Pal, S., Bončina, T., Lojen, G., Brajlih, T., Fabjan, E.Š., Gubeljak, N., ... & Drstvenšek, I. (2024), "Fine martensite and beta-grain variational effects on mechanical properties of Ti–6Al–4V while laser parameters change in laser powder bed fusion", *Mater. Sci. Eng.: A*, **892**, 146052. https://doi.org/10.1016/j.msea.2023.146052.

Park, S., Clayton, P., Helwig, T.A., Engelhardt, M.D. and Williamson, E.B. (2024), "Experimental investigation of local stress distribution along the cross-section of composite steel beams near joints", *Steel Compos. Struct.*, **51**(5), 563-573. https://doi.org/10.12989/scs.2024.51.5.563.

Prabhu, S., Sri, M.N.S., Anusha, P., Saravanan, G., Kannan, K. and Manickam, S. (2022), "Improvement of mechanical behavior of FSW dissimilar aluminum alloys by postweld heat treatments", *Adv. Mater. Sci. Eng.*, **2022**(1), 3608984. https://doi.org/10.1155/2022/36089.

Raoelison, R.N., Sapanathan, T., Li, J.S., Zhang, Z., Racine, D., Chen, X.G., ... & Rachik, M. (2023), "Transformation sequence of Mg-Si precipitates towards a precipitation of Mn and Cr containing phase governed by the high strain-rate collision during magnetic pulse welding of Al-Mg-Si alloy", *J. Alloy. Metal. Syst.*, **4**, 100048. https://doi.org/10.1016/j.jalmes.2023.100048.

Tian, Y., Tan, Z., Zhang, J., Yuan, Z., Zhang, X., Zhang, Z. and Zhang, M. (2023), "Microstructure stability in wheel steel: A case of thermal-accumulated damage capacity in pearlite and low-carbon bainite", *Eng. Fail. Anal.*, **154**, 107656. https://doi.org/10.1016/j.engfailanal.2023.107656.

Vemanaboina, H., Edison, G., Akella, S. and Buddu, R.K. (2018), "Thermal analysis simulation for laser butt welding of Inconel625 using FEA", *Int. J. Eng. Technol*, **7**(4.10), 85.

Xie, X., Yu, D., Chen, J., Liang, Z. and Wang, J. (2024), "Enhancement of high-temperature fatigue properties of 310S stainless steel welded joints by strengthened grinding process inducing gradient structure", *Eng. Fail. Anal.*, **157**, 107846. https://doi.org/10.1016/j.engfailanal.2023.107846.

Zhang, Z., Feng, Y., Zhang, D. and Pan, Z. (2024), "Application of a ductile connection system to steel MRF strengthened with hinged walls", *Steel Compos. Struct.*, **51**(5), 487-498. https://doi.org/10.12989/scs.2024.51.5.487.

CC

Apendex-A: Python Code for failure envolop

```
import numpy as np
import matplotlib.pyplot as plt
sy=283.32  # yeild strength those from conducting Experiment
s1=0  # principal stress 1, s1
s2=0  # principal stress 2, s2
class MaterialFailure():
    def __init__(self,sy,s1,s2):
        ‘‘‘ INPUT INITIAL INFORMATION
              σ_y : sigma y
              σ_1 : sigma 1
              σ_2 : sigma 2
        self.sy=sy
        self.s1=s1
        self.s2=s2
    def vonMisesCriterionPlot(self):
        s_von=np.sqrt(self.s1**2 + self.s2**2 -(self.s1-self.s2))
        a=np.sqrt(2)*self.sy
        b=np.sqrt(2/3)*self.sy
        alpha=np.linspace(0,2*np.pi,360)
        theta=np.pi/4 # 45degree
        x=(a*np.cos(alpha)*np.cos(theta)) - (b*np.sin(alpha)*np.sin(theta))
        y=(a*np.cos(alpha)*np.sin(theta)) + (b*np.sin(alpha)*np.cos(theta))
        x1=[252.987,337.356,421.3658,505.97,590.3] #sigma- from ANSYS
        y1=[74.62,99.5046,124.38,150,174.6985]      #sigma-2 from ANSYS
        # set graph size
        #plt.figure(figsize=(10,8))
        plt.title("Von Mises Failure Envolop for SS-GI",fontsize=20)
        plt.xlabel(r’$\sigma_1$’,fontsize=14)
        plt.ylabel(r’$\sigma_2$’,fontsize=14)
        plt.fill_between(x,y,color=‘r’,hatch=‘\\’,alpha=0.1)
criterion)
        plt.plot([self.sy,self.sy],[0,sy],’r--’)
        plt.plot([0,self.sy],[self.sy,self.sy],’r--’)
        plt.plot([-self.sy,0],[-self.sy,-self.sy],’r--’)
        plt.plot([-self.sy,-self.sy],[0,-self.sy],’r--’)
        plt.plot([0,-self.sy],[self.sy,0],’r--’)
        plt.plot([self.sy,0],[0,-self.sy],’r--’)
        # Create horizontal and vertical lines at center
        plt.axhline(color=‘k’)
        plt.axvline(color=‘k’)
        plt.scatter(x1, y1, color=‘g’)
              plt.grid(‘true’)

"Failure Envolop", ‘1’], fontsize=12)
```

```
        plt.show()

if __name__ == '__main__':
    x=MaterialFailure(sy,s1,s2)
    x.vonMisesCriterionPlot()
```